Journal of Applied Physics

RESEARCH ARTICLE | SEPTEMBER 03 2024

Stress field measurements using quantitative schlieren

S. M. Torres ; J. Kimberley ; M. J. Hargather

J. Appl. Phys. 136, 095102 (2024)
https://doi.org/10.1063/5.0223560
CHORUS

AIP Publishing

Journal of Applied Physics ARTICLE pubs.aip.org/aip/jap

Stress field measurements using quantitative schlieren

Cite as: J. Appl. Phys. **136**, 095102 (2024); doi: 10.1063/5.0223560
Submitted: 15 June 2024 · Accepted: 14 August 2024 ·
Published Online: 3 September 2024

S. M. Torres, J. Kimberley, and M. J. Hargather[a)]

AFFILIATIONS

Department of Mechanical Engineering, New Mexico Tech, 801 Leroy Pl, Socorro, New Mexico 87801, USA

[a)]**Author to whom correspondence should be addressed:** michael.hargather@nmt.edu

ABSTRACT

Quantitative schlieren analysis is extended here to optically transparent solids in quasi-static and dynamic experiments to measure stress distributions. The quasi-static experiments in polymethyl methacrylate (PMMA) compared refraction angles and stress gradients calculated from schlieren images to the analytical Flamant solution of a line load on a half-space. The quantitative schlieren measurements of the stress field in the thin sample with a load compared well to the analytical solution. The analysis method was then extended to explosive induced shock waves in PMMA. The explosive induced response of PMMA was experimentally studied using high-speed schlieren to visualize the shock propagation in conjunction with Photon Doppler Velocimetry (PDV) to record surface velocity histories. The stress state estimated from the schlieren images was compared to the stress calculated from the PDV measurements. High-speed imaging limitations caused the shock wave to not be fully resolved in the images, but was resolved in the PDV measurement. The stress state behind the shock calculated from the high-speed images followed a similar trend to the stress calculated from the PDV measurements.

I. INTRODUCTION

When a transparent material is externally stressed, the refractive index of the material changes due to the induced stresses. Maxwell formulated the stress-optic law which relates a material's refractive indices to the principal stresses.[1] The stress-optic law is based on the proportionality of the indices of refraction and the principal stresses for temporarily birefringent materials. The refractive index change is indicative of an optical path length change; thus, the stress-optic law can be leveraged to calculate stresses and strains in materials which portray a change in refractive index due to induced stresses using the change in optical path length. It is important to note that deformation also contributes to a change in optical path length of the transmitted light rays. The implementation of the stress-optic law to calculate the stresses and strains in a material is not limited to temporarily birefringent materials, it has also been extended to optically isotropic materials.[1–3] Methods such as photoelasticity,[1] the shadow optical method of caustics,[4,5] coherent gradients sensing (CGS),[6,7] and digital gradient sensing[2,3] are a few examples of methods which leverage the stress-optic law. Photoelasticity is the only method in which birefringence is required for the optical method to work, and the other methods utilize the stress-optic law for both birefringent and optically isotropic materials. These experimental methods are widely used in the study of fracture mechanics.

Photoelasticity is ideal for full-field optical analysis; however, difficulties can arise with measurement of stress singularities.[8] For stress singularities, like crack tips, analysis of isocromatic fringe patterns is non-ideal. The introduction of the optical method of caustics introduced an alternative method for quantifying stress concentration problems.[1,8] Unlike photoelasiticity, the optical method of caustics is not a full-field method and has a simple arrangement because the method is based on the law of refraction of geometric optics. All that is required is an illumination source and a reference screen.[8] The light from the illumination source propagating through, or reflecting off, a deformed specimen will be deflected from the original light path creating a shadow pattern. Then, the evaluation of the shadow patterns can be applied to solve stress concentration problems.[1] This method is typically implemented for the determination of stress intensity factors around crack tips in which only the diameter of the caustic is needed.[5] The method of caustics leverages the stress-optic law which has been utilized for other optical analysis methods such as coherent gradient sensing (CGS).

Coherent gradient sensing (CGS) is a full-field optical technique developed by Tippur *et al.*[9] to measure surface slopes or in-plane stress gradients.[7] With the similarity to the optical method of caustics, it was extended to quantification of crack tip deformations.[7,10] This method is a lateral shearing interferometry technique in which a first order diffraction analysis is used.[9] The optical arrangement consists of light propagating through, or reflecting off, a specimen, two Ronchi gratings, a filtering lens, and a camera. The Ronchi gratings and the filtering lens create the interference pattern. This method is widely used for static and dynamic fracture analysis.[6,7,11] The mapping of the deflected light ray's angular deflection to the mechanical field used for CGS was then extended to digital gradient sensing (DGS).

Digital gradient sensing (DGS) is a full-field method for measuring small light deflections due to local stress gradients in optically transparent materials.[3] Digital gradient sensing relates the refraction angles to the principal stress gradients based on the same relations used for CGS. The stress gradients parallel and perpendicular to a line load applied to the sheet of PMMA were experimentally measured and compared to the analytical Flamant solution.[3] The method was also extended to dynamic experiments, where a PMMA sample was dynamically loaded with a line load and was again validated against the Flamant solution.[2] The solution to the Flamant problem yields an analytical solution for stresses and displacements for a body subjected to a line load in a half-space. Both the static and dynamic experiments were in good agreement with the analytical solution.

The DGS method is similar to background oriented schlieren (BOS)[12–14] in that both methods leverage a speckled background to detect changes caused by disturbances in the object plane. Both methods utilize Digital Image Correlation (DIC), or similar analysis methods,[15] to determine how a speckle pattern on a background appears to have been displaced. The apparent displacement is then related to a refraction angle which can then be used to calculate optical properties of the disturbance. BOS is a type of schlieren imaging, which is a class of refractive imaging techniques commonly applied in fluid dynamics[12,16] to visualize refractive index variations in flows containing density or gas species variations. In schlieren imaging, the refraction angles of a light ray are proportional to the refractive index gradient.[16] Refraction angles are measured and converted to refractive index gradient fields, which are then integrated to yield the refractive index field which can be related to a density field in the medium.[17]

For schlieren images, the relationship between index of refraction and refraction angle is based on the gradient of the refractive index being proportional to the angle of the bent light rays. Classical schlieren uses a collimated light source, focusing optics, and a knife-edge cut-off to produce images with intensity variations related to the angles of refraction. Light rays refracted toward the cut-off result in a reduction in intensity, conversely refraction away from the knife edge result in increases in intensity. Quantitative schlieren techniques have been applied to experiments with objects of a fixed length[17] and for spherically symmetric objects like shock waves using the Abel transform.[18] Pressure and temperature measurements using the calculated density have also been demonstrated.[17,18] The densities calculated from quantitative schlieren analysis in air leverage the Gladstone–Dale relationship. In the literature, quantitative schlieren has not been demonstrated as a method to image stress fields in transparent solids, which is the focus of the work here.

Quantitative schlieren analysis is extended here using the stress-optic law to estimate stresses using the measured refraction angle in PMMA. The method is validated using quasi-static experiments for comparison to the analytical Flamant solution. The quantitative schlieren analysis method was then extended to experiments where an explosively driven shock wave propagated through a PMMA sample.

II. GOVERNING EQUATIONS

Compression of a material increases the thickness of the body due to the Poisson effect, and the inverse is true for a body in tension. The change in thickness causes a change in optical path length. The optical path length is changed because the light ray travels through more of the material. The stresses imparted by an external load also cause a change in refractive index of the material which also can result in a change in the optical path length. Accounting for both of these effects, the optical path length change (Δs) caused by deformation can be represented as[1]

$$\Delta s = (n_0 - 1)\Delta d_e + d_e \Delta n, \tag{1}$$

where n_0 is the refractive index of the undisturbed material, Δd_e is the change in effective thickness of the material, d_e is the effective thickness of the material, and Δn is the change in refractive index. Refractive index can vary with the direction in solids, and for birefringent materials, the indices of refraction are related to the principal stresses through the the Maxwell–Newmann law,

$$\Delta n_x = A_c \sigma_x + B_c(\sigma_y + \sigma_z), \tag{2}$$

$$\Delta n_y = A_c \sigma_y + B_c(\sigma_x + \sigma_z), \tag{3}$$

$$\Delta n_z = A_c \sigma_z + B_c(\sigma_x + \sigma_y), \tag{4}$$

where Δn_x, Δn_y, and Δn_z are the change in refractive indices in the x-, y-, and z-directions, respectively, A_c and B_c are the stress-optic constants, and σ_x, σ_y, and σ_z are the principle stress in their respective directions. Generalized Hooke's law describes Δd_e for propagation in the z-direction in terms of the normal stresses as[1]

$$\Delta d_e = \frac{1}{E_y}\left[\sigma_{zz} - \nu(\sigma_{xx} + \sigma_{yy})\right] d_e, \tag{5}$$

where ν and E_y are Poisson's ratio and Young's modulus for the material, respectively. Equations (1)–(5) can then be used to define the optical path length change caused by external stress in the respective directions. For PMMA, the stress-optic coefficients are approximately equal, $A_c \approx B_c$ implying optical isotropy; thus, the two values were averaged in the present work to obtain an isotropic stress-optic coefficient D_c. In this arrangement, x and y are planar coordinates and z the coordinate in the imaging direction. For a two-dimensional plane stress case, ($\sigma_{zz} = 0$), only the optical path

length change in the x- and y- directions are considered. The optical path length change is, thus,

$$\Delta s = d_e C_\sigma [\sigma_{xx} + \sigma_{yy}], \tag{6}$$

where

$$C_\sigma = D_c - \frac{\nu(n_0 - 1)}{E_y}. \tag{7}$$

The values σ_{xx} and σ_{yy} are the normal stress components averaged over the thickness of the sample.[3,7] The elasto-optic coefficient, C_σ, accounts for the change in optical path length due to both the refractive index change and Poisson effect as described by Eq. (1).[7] The presented equations are the governing equations for experimental techniques, including Coherent Gradient Sensing (CGS),[7,10] the optical method of caustics,[1] and Digital Gradient Sensing (DGS),[2,3] and will be shown here to hold for schlieren as well. The unit light propagation vector, $\hat{d}$, for a perturbed light ray is then related to the change in optical path length, Δs, through[3,7,10]

$$\hat{d} \approx \frac{\partial(\Delta s)}{\partial x}\hat{i} + \frac{\partial(\Delta s)}{\partial y}\hat{j} + \hat{k}. \tag{8}$$

The unit light propagation vector is defined in Cartesian coordinates with $\hat{i}$, $\hat{j}$, and $\hat{k}$ being unit vectors in the x, y, and z directions, respectively. As such, the unit vector $\hat{k}$ for an undisturbed system is parallel to the imaging direction. The relationship presented in Eq. (8) is for the case of small angular deflections and small stress gradients. The relationship between the light propagation vector and the optical path length change is then used to relate the optical path length change to refraction angle as described by Periasamy and Tippur.[3] The resulting relationship is

$$\varepsilon_x \approx \frac{\partial(\Delta s)}{\partial x} \approx d_e C_\sigma \frac{\partial(\sigma_{xx} + \sigma_{yy})}{\partial x}, \tag{9}$$

$$\varepsilon_y \approx \frac{\partial(\Delta s)}{\partial y} \approx d_e C_\sigma \frac{\partial(\sigma_{xx} + \sigma_{yy})}{\partial y}. \tag{10}$$

These equations are the governing equations for obtaining the stress gradients from schlieren images. The refraction angles, ε_x and ε_y, are measured through calibration of the schlieren imaging system.[17,18]

III. THE ANALYTICAL FLAMANT SOLUTION

The Flamant solution provides an analytical expression of the stresses throughout a linear elastic, homogeneous, isotropic body subjected to a line load in an elastic half-space[19] as depicted in Fig. 1. For a normal force, F, acting in the y-direction, there exists a simple stress distribution.[20]

Any element, r_{xy}, which is a distance r from the load, undergoes a compression in the radial direction. The stress components for the compression of a body having a thickness of d_e are given in polar coordinates,[3,20]

$$\sigma_{rr} = -\frac{2F}{\pi d_e}\frac{\cos\theta}{r}, \tag{11}$$

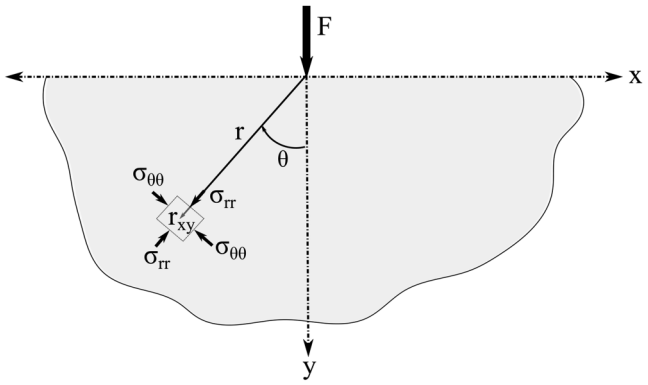

FIG. 1. Schematic of an elastic half-space loaded with a point load.

$$\sigma_{\theta\theta} = 0, \tag{12}$$

$$\sigma_{r\theta} = 0. \tag{13}$$

The Hoop stress $\sigma_{\theta\theta}$ and shearing stress $\sigma_{r\theta}$ are zero, satisfying the equilibrium equation. The relationship between σ_{rr} and $(\sigma_{xx} + \sigma_{yy})$ for the Flamant solution is[20]

$$(\sigma_{xx} + \sigma_{yy}) = \sigma_{rr}(\cos^2\theta + \sin^2\theta) = \sigma_{rr}. \tag{14}$$

A light ray passing through the stress field will be distorted according to Eqs. (9) and (10). For the Flamant solution, the light ray angular deflections in the x- and y-directions, respectively, become

$$\varepsilon_x = d_e C_\sigma \frac{\partial(\sigma_{rr})}{\partial x}, \tag{15}$$

$$\varepsilon_y = d_e C_\sigma \frac{\partial(\sigma_{rr})}{\partial y}. \tag{16}$$

Substituting Eq. (11) into the above equations, the analytical solutions for ε_x and ε_y are

$$\varepsilon_x = d_e C_\sigma \frac{2F}{\pi d_e}\frac{\sin 2\theta}{r^2}, \tag{17}$$

$$\varepsilon_y = d_e C_\sigma \frac{2F}{\pi d_e}\frac{\cos 2\theta}{r^2}. \tag{18}$$

IV. EXPERIMENTAL METHODS

Schlieren imaging is used to visualize the first spatial derivative of refractive index in optically transparent materials.[12,16] The schlieren effect requires the implementation of a knife-edge cut-off. Without the cut-off, the imaging technique visualizes the Laplacian of the refractive index and is referred to as focused shadowgraphy.[16]

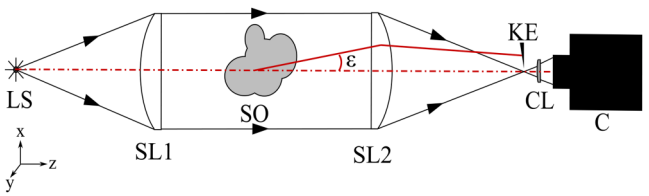

FIG. 2. Schematics of a lens-type schlieren system.

A schematic of a lens-type schlieren imaging system is shown in Fig. 2. The lens based system utilizes achromatic doublets as the schlieren optics SL1 and SL2. Light from a point light source is collected by SL1 collimating the light. After the test section, the collimated light is recollected and refocused using a second schlieren optic SL2. The refocused light creates a point, having a diameter equivalent to the original light source, one focal length from SL2 where the knife-edge (KE) cut-off is placed to produce the schlieren effect. The light is then collected and the schlieren object is imaged by a camera which is focused to the schlieren object location.

In a schlieren imaging system, the refraction angle of a light ray is proportional to the refractive index gradient. For a light ray propagating in the z-direction with the light refracted in the x-direction, ε_x is generally represented as[16,17]

$$\varepsilon_x = \frac{1}{n}\int \frac{\partial n}{\partial x}\partial z. \tag{19}$$

The integration is performed over the extent of the schlieren object where the refractive index gradient is considered to exist. For a two-dimensional schlieren object having a thickness in the z-direction of d, this reduces to

$$\varepsilon_x = \frac{d}{n_0}\frac{\partial n}{\partial x}, \tag{20}$$

where n_0 is the refractive index of the undisturbed medium. Bent light rays are visualized in the schlieren imaging system as a change in the pixel intensity. Depending on the direction, the ray is bent and an individual pixel will either experience an increase or decrease in the pixel intensity due to the interaction with the knife-edge cut-off.

PMMA was selected as the specimen material to match previous works[2] and has well defined optical properties. The material constants used here for PMMA are presented in Table I. The

TABLE I. PMMA constants used for quantitative schlieren analysis.

PMMA constant	Value	Units
A_c[1]	-0.530×10^{-10}	m^2/N
B_c[1]	-0.570×10^{-10}	m^2/N
n_o	1.49	
ν	0.35	
E_y	2.8×10^9	Pa

PMMA samples used in the present work were cast sheets of PMMA purchased from Boedeker Plastics. The imaging surfaces were used as delivered. The samples were cut to the length and height as described below.

A. Experimental methods for quasi-static experiments

Quantitative schlieren analysis was applied to PMMA samples which were quasi-statically compressed using a Mark-10 Motorized Force Tester. The PMMA sample had a thickness of 9.4 mm, a length of 177.8 mm, and a height of 88.9 mm. The sample geometry was selected such that a plane stress assumption could be made and it was similar to previous works.[3] The sample also had to be thin enough to minimize light ray perturbations caused by the unstressed PMMA. The sample length and width allowed for a semi-infinite body assumption. The base of the sample was stabilized using a piece of aluminum on the bottom compression head which supported the length of the PMMA sample.

To create the point load in the imaging plane, a 4-mm-diameter steel pin was attached to the top compression head. The PMMA was placed in the Mark-10 such that the loading pin was centered along the length of the PMMA sample as shown in Fig. 3. The Mark-10 compression head speed was set to the minimum, 0.167 mm/s. The load cell used to measure the applied force was a series R01 tension and compression force sensor. The force as a function of time was recorded with a sample rate of 50 Hz.

The PMMA specimen was centered in the schlieren imaging system test section. The schlieren system was a simple lens-type schlieren system which was set up in line with the Mark-10 as shown in Fig. 4. The schlieren lenses had focal lengths of 400 mm (f/# ≈ 4), and a white LED light was used as the light source. The camera used to record the event was a Photron Nova operating at a frame rate of 50 fps which matched the sample rate of the force measurements. Two knife-edge cut-off orientations, vertical and horizontal, were studied separately allowing for the calculation of refraction angles in horizontal (x) and vertical (y) directions.

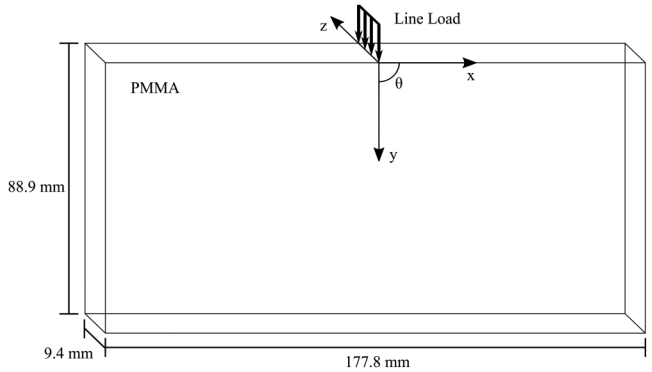

FIG. 3. A schematic of the PMMA sample with dimensions and the location of the applied force.

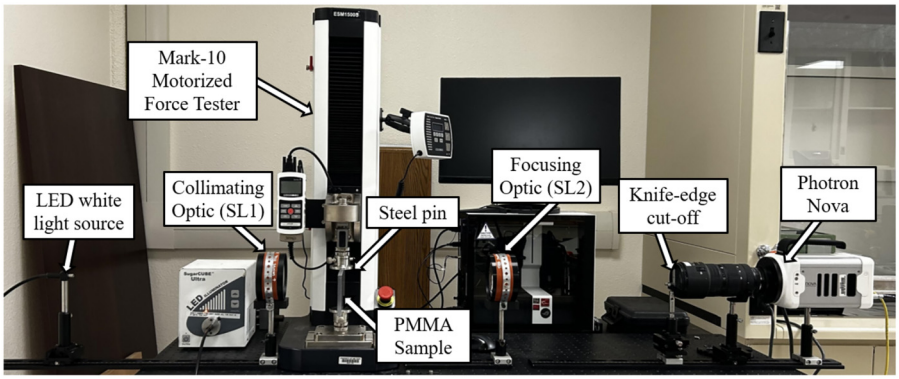

FIG. 4. Image of the quasi-static experimental setup.

The schlieren imaging system sensitivity is dependent on the amount of light that is being cut-off. The amount of cut-off was determined using a plano–convex calibration lens, with a 2 m focal length as shown in Fig. 5. The focal length of the calibration lens is of particular importance and should be selected such that the focal length of the calibration lens is longer than the distance from the object to the cut-off. If the calibration lens focal length is too long, then the full range of grayscale values will not be visible; thus, the system dynamic range is not fully calibrated. The schlieren system dynamic range is set by the focal length of the schlieren optic SL2 and the system geometry.[17] For the experiments here, the PMMA specimen thickness and loading conditions were chosen so that the expected refractions were within the dynamic range of the schlieren system.

B. Experimental methods for explosive experiments

To quantify the explosively driven material response of PMMA, two synchronized high-speed cameras were used to image the event. The two high-speed cameras were Shimadzu HPV-X2s which recorded at 2 Mfps. The light source was a SI-LUX pulsed laser, with a pulse width of 15 ns. The laser had a wavelength of 640 nm allowing for a bandpass filter of the same wavelength to be placed in front of the cameras, reducing external illumination from the detonation event. The explosive was an RP-80 EBW detonator placed in contact with the PMMA as shown in Fig. 6. Silicone grease was placed on the interface between the PMMA and the detonator face to improve the contact between the two materials.

The PMMA sample was the same thickness as the quasi-static experiments, 9.4 mm, which was also approximately the diameter of the detonator. The length and width of the sample were both 88.9 mm. Surface velocity measurements were made on the surface opposite of the detonator using Photon Doppler Velocimetry (PDV).[21] The PDV data were analyzed with the SIRHEN analysis software.[22] A piece of retro-reflective tape was placed on the surface where the PDV measurement was taken. The explosive event was contained in a boom box, as shown in Fig. 7. The specimen was centered in the parallel light schlieren system test section. Optical glass was used as the window material in order to reduce distortions in the parallel light test section. The same schlieren lenses used for the quasi-static experiments were used for the dynamic

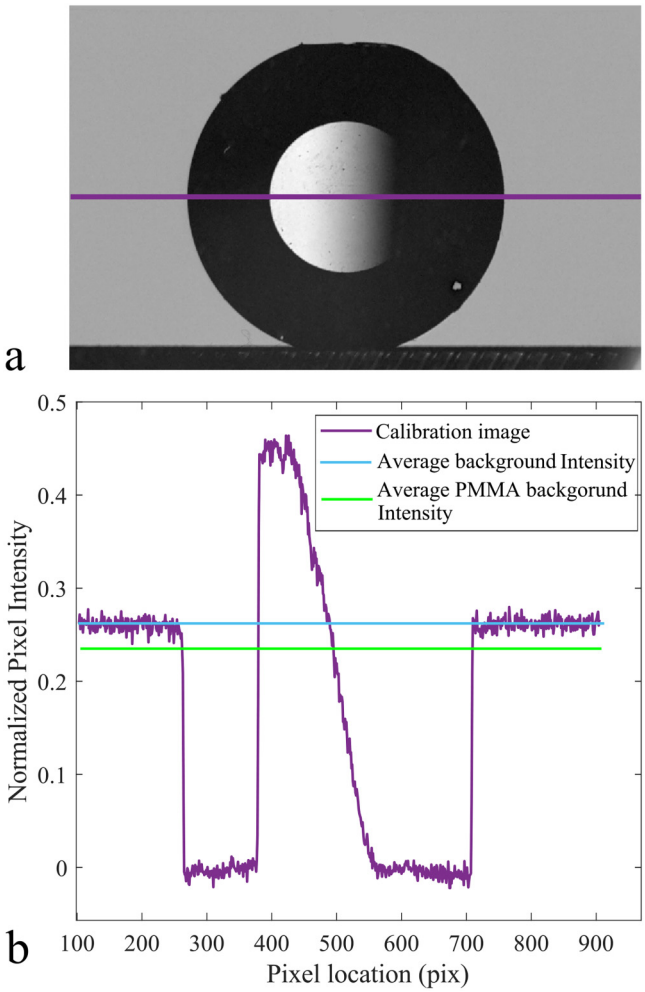

FIG. 5. (a) An image of a plano–convex calibration lens with a vertical knife-edge cut-off and (b) a plot of the pixel intensity values as a function of position for the purple line in (a) and the average background intensity with (green line) and without (blue line) PMMA.

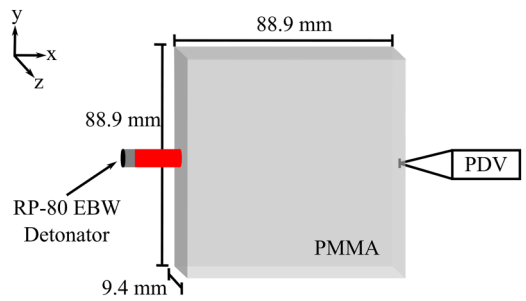

FIG. 6. Schematic of the PMMA sample used for the explosively loaded PMMA experiments.

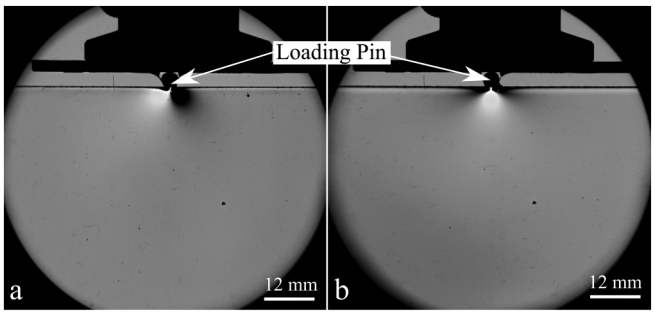

FIG. 8. (a) Vertical knife-edge and (b) horizontal knife-edge schlieren images of the PMMA sample subject to a line load of 2365 N.

tests. After the focusing optics, prior to the focal point, the light path was split toward the two different cameras using a beam splitter cube. The two cameras had different knife-edge cut-offs, one vertical and one horizontal. An image of the experimental setup is shown in Fig. 7.

V. DATA ANALYSIS

The application of external force introduced grayscale intensity variations in the PMMA when imaged in the schlieren system. In order to quantify the stress gradient from the external force, vertical and horizontal refractions were measured. The knife-edge direction dictates the direction of the refraction angle being measured, with a horizontal knife-edge measuring vertical refractions and vertical knife-edge measuring horizontal light refractions.[16] Representative schlieren images of the grayscale intensity variations experimentally observed from quasi-static loading are shown in Fig. 8.

A. Explosive experiment data synchronization

Two high-speed cameras were used to image the explosive event to measure the displacements in the x- and y- directions synchronously. The two cameras were synchronized in time, however, the spatial alignment was off slightly. The alignment of the two data sets was achieved using image registration in MATLAB. A marker was placed on the PMMA samples prior to testing with the intent of aligning the two image sets as shown in Figs. 9(a) and 9(b). The marker also indicates the y-location of the PDV measurement.

B. Calculating refraction angle from pixel intensity

Two cut-off directions were used to calculate vertical (y-direction) and horizontal (x-direction) displacements. A horizontal cut-off allows for the refraction angles in the y-direction, ε_y, to be calculated, whereas a vertical cut-off allows for the refraction angles in the x-direction, ε_x, to be calculated. The refraction angles are calculated through calibration of the imaging system grayscale intensities to a known refraction angle. This was done using a weak positive focal length lens as the calibration object. The calibration lens used for both the quasi-static and dynamic tests was a plano–convex lens with a focal length of 2m purchased from CVI laser optics (part No.: PLCX-25.4-1030.2-C). Images of the calibration lens with the vertical and horizontal cut-off are presented in Figs. 10(a) and 10(c), respectively.

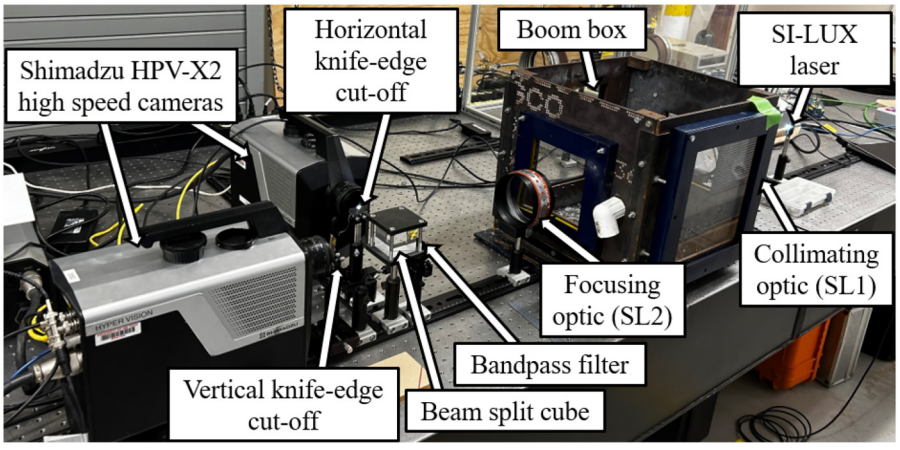

FIG. 7. Image of the experimental setup used for conducting the explosively loaded PMMA experiments.

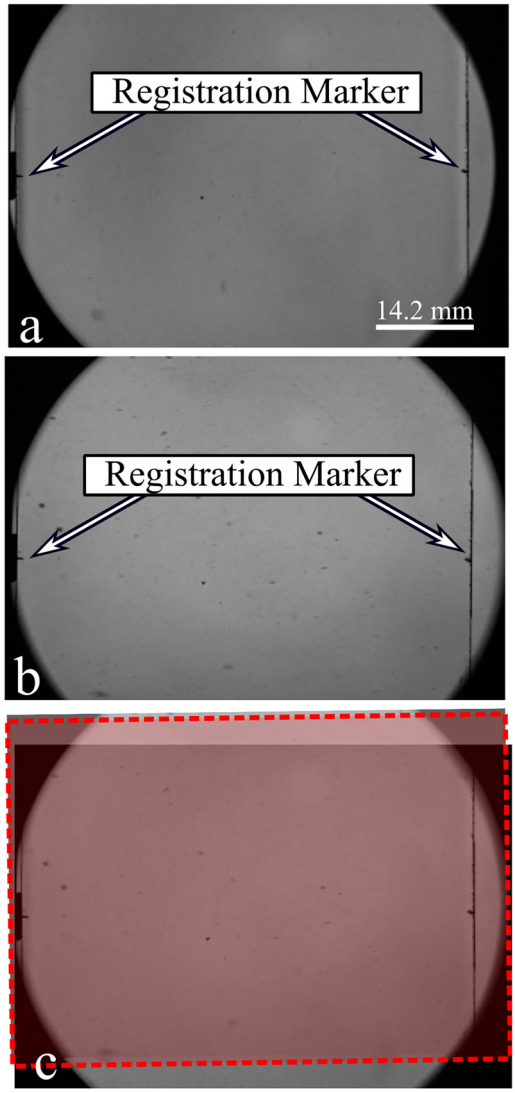

FIG. 9. Images of data collected from the camera with (a) a vertical cut-off, (b) a horizontal cut-off, and (c) the two images aligned using the marker.

A gradient of "light" pixels to "dark" pixels was captured in the calibration lens. The grayscale value of the pixels is referred to as the pixel intensity. The calibration lens was used to relate pixel intensity to refraction angle, ε, using the light to dark gradient of pixel intensities in the center of the calibration lens. Figure 10 shows schlieren images of the calibration lens for a vertical [Fig. 10(a)] and horizontal [Fig. 10(c)] cut-offs. In Fig. 10(a), the horizontal row of pixels across the image and through the center of the calibration lens is highlighted with the purple line and the pixel intensities along that line are plotted in Fig. 10(b) as the purple line. To reduce noise due to camera pixel intensity fluctuations, five rows of pixels along the centerline [outlined in orange in Fig. 10(a)] were averaged to create an average pixel intensity vs position in the lens. These average data were fit to a polynomial such that the pixel location in the calibration lens, R_x, was a function of the pixel intensity, I. Fitting the data in this manner allows for determination of the location in the calibration lens from a pixel intensity value. The same process was applied to the horizontal cut-off image in Fig. 10(c) using five columns of pixels and yielding R_y as a function of I.

The location in the calibration lens, R_x and R_y indicated as the orange lines in Figs. 10(b) and 10(d), is used to calculate the refraction angle for a specific intensity value. First, the average background intensity for the uncompressed PMMA sample was calculated from the image and its value is plotted as the green dotted-dashed line in Figs. 10(b) and 10(d). The lens location (r_{PMMA}) corresponding to this intensity value was determined using the polynomial fit to the calibration lens data. This average PMMA background intensity was taken as a value of zero refraction ($\varepsilon = 0$). Once the location of zero refraction was known, then the lens geometry was used to calculate the refraction angles.[17]

Calculating a vertical refraction angle, ε_y, for an arbitrary perturbed light ray begins with the pixel intensity of the light ray from the image. The intensity of the perturbed light ray, I_p, was then used to determine, where in the calibration lens, the same pixel intensity value exists using the polynomial fit, $R_y(I_p)$. The location of the pixel value inside the calibration lens, R_y, then allows for the calibration lens geometry to be used to calculate the refraction angle, ε_y. The ray displacement, r_y, depicted in Fig. 11 was calculated using the location in the calibration lens, R_y, relative to the location of zero refraction, r_{PMMA},

$$r_y = R_y - r_{PMMA}. \tag{21}$$

Then, r_y and the focal length of the calibration lens f were used to calculate ε_y using trigonometry,

$$\varepsilon_y = \arctan\frac{r_y}{f}. \tag{22}$$

The same analysis was applied to the vertical cut-off images in order to calculate ε_x. Note, the amount of cut-off for the two cameras does not need to be exactly the same. Ideally, the two cameras would image the same dynamic pixel intensity range; however, it is not required.

VI. EXPERIMENTAL RESULTS AND DISCUSSION

A. Quasi-static experiments

The Mark-10 force data and the schlieren images were synchronized such that at each force there was a corresponding schlieren image. A force of 2365 N was selected for the analysis. The refraction angles in the schlieren images were calculated using the pixel intensities in the image. The raw schlieren image with a vertical knife-edge cut-off is presented in Fig. 12(a) and the resulting refraction angles are presented in Fig. 12(b). For comparison to the analytical solution, the refraction angles were plotted using the MATLAB function *contour* with contour levels of $-5:1:5$ mrad creating isolines shown in Fig. 12(c). The isolines created from the

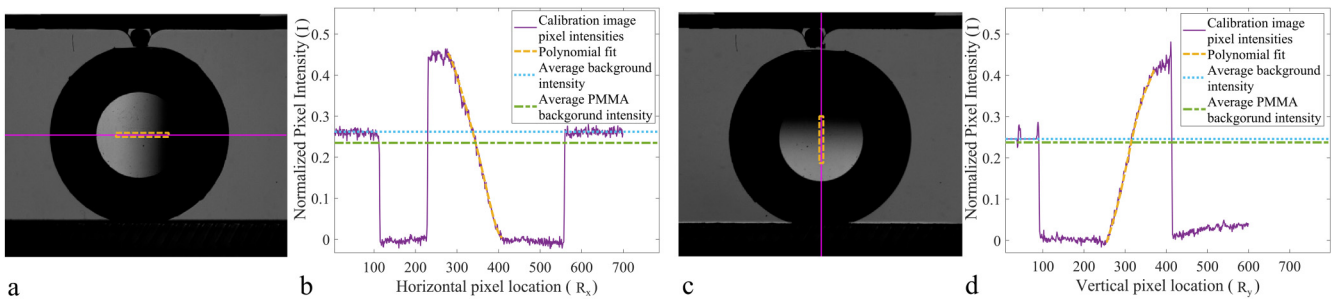

FIG. 10. Images of the calibration lens with (a) a vertical knife-edge cut-off and (c) a horizontal knife-edge cut-off with (b) and (d) corresponding plots of (solid purple lines) pixel intensities as a function of location, the polynomial fit to the calibration data (dashed orange lines), the average background pixel intensity without PMMA (double dashed blue lines), and the average background pixel intensity of the PMMA (dashed-dotted green lines).

refraction angles follow the same shape that was created from the grayscale pixel intensity variation in the raw schlieren images, which was expected. The isolines for ε_x reveal a slight asymmetry [Fig. 12(c)]. The isolines in the positive x-direction are slightly larger than the isolines in the negative x-direction. The zero refraction line between the two isolines is also biased slightly in the negative x-direction. The bias direction was more apparent when comparing the experimental solution to the analytical solution presented in Fig. 13(a). Note that all data are aligned with the load applied at the origin location.

The analytical refraction angles were calculated using Eqs. (17) and (18). The analytical solution was plotted in the same manner as the experimental refraction angles, creating isolines. The isolines from the analytical solution (black lines) were plotted over the experimental isolines (colored lines) resulting in the plots in Fig. 13.

Relative to the analytical solution, the zero refraction angle for ε_x [Fig. 13(a)] was slightly inclined in the negative x-direction. This could potentially be due to a small misalignment of the sample not being perfectly perpendicular to the collimated schlieren light. The variation, though, is also within the error of the quantitative measurement based on the individual pixel intensity variation noise as discussed below. Comparing the experimentally determined isolines for ε_y to the analytical solution reveals agreement between the two solutions with no observed asymmetry.

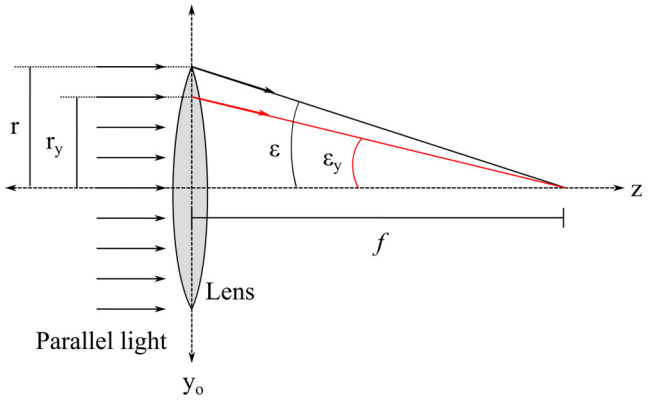

FIG. 11. Schematic of a calibration lens.

It is expected that the analytical solution and experimental solution up to $r/d_e = 1/2$ will differ because the plane stress assumptions are violated close to the loading point where a zone of dominant triaxiality exists.[3] There are also isolines that appear close to the sample boundary which are caused by boundary effects from the manufacturing of the PMMA samples. Images of the experimental solution compared to the analytical solution with the zone of dominant triaxiality highlighted in red and the boundary effects highlighted in gray for three different load cases of (a) and (d) 2365 N $\pm$5 N, (b) and (e) 1860 N $\pm$5 N, (c) and (f) 1360 N $\pm$5 N are presented in Fig. 14.

The zone of dominant triaxiality for the present experiments had a radius of approximately 4.6 mm. Comparing the experimental results to the analytical solution for the three different load cases, it can be seen that outside of the zone of dominant triaxiality the two are in good agreement. As expected, the isoline sizes increase with an increase in compressive force. For the vertical cut-off experiments [Figs. 14(a)–14(c)], the experimental results align well with the analytical solution despite the asymmetry. The isolines in the negative x-direction are slightly smaller than the isolines in the positive x-direction. The asymmetry appears to have a more significant impact on the outer isolines, $\varepsilon_x = \pm 0.001$ radians, with the asymmetry being more apparent for the lower load (c). The inner isolines, ± 0.002 radians and ± 0.003 radians, do not appear to be asymmetric and align well with the analytical solution.

The horizontal cut-off images had two lines of zero refraction. The two lines of zero refraction for the experiment and analytical solution aligned. For these experiments, the measurement was in agreement with the analytical solution for the outer isoline at an angle of 0.001 radians. However, for the isolines at an angle of 0.002 radians ,there was slight misalignment attributed to the calibration data. The calibration pixel intensities did not span the full dynamic range of the camera and the intensities observed in the images. The center isolines were calculated from the light side of the calibration image. The pixel intensity range imaged by the

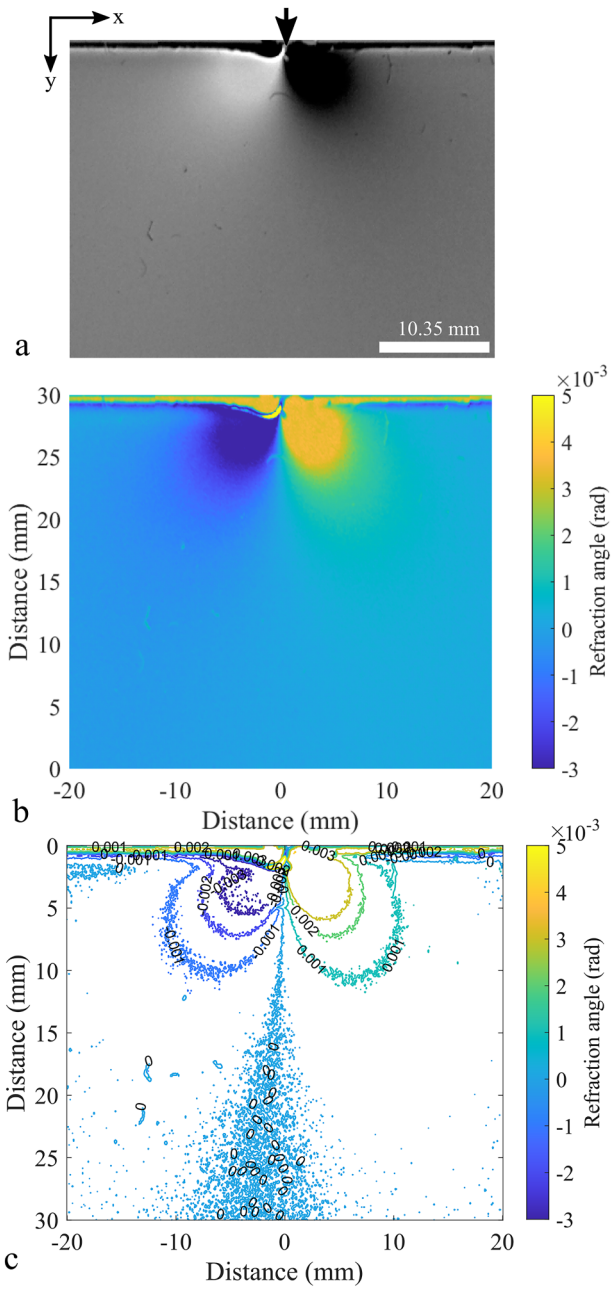

FIG. 12. (a) A schlieren image with a vertical knife-edge cut-off with a line load having a force of approximately 2365 N with (b) the resulting refraction angles and (c) isolines created using a contour plot.

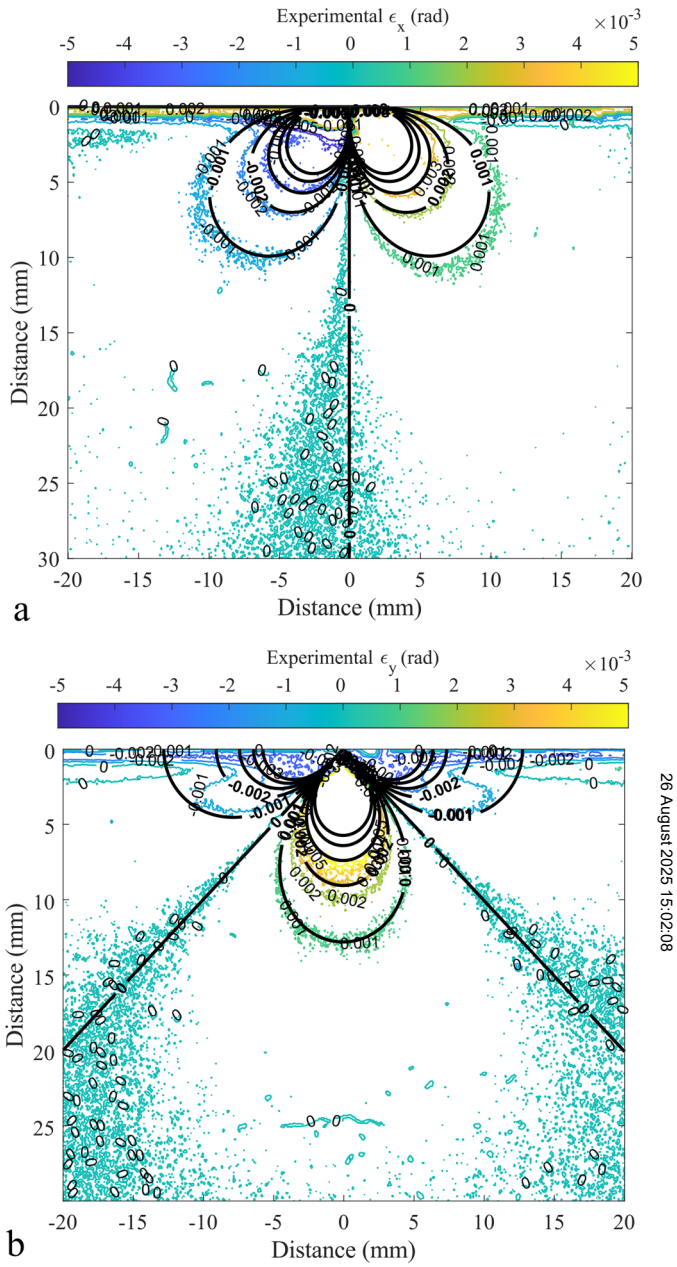

FIG. 13. The experimental refraction angles (colored contours) for (a) refraction angles in the x-direction (ϵ_x) and (b) refraction angles in the y-direction (ϵ_y) compared to the analytical solution (black lines).

calibration lens ranged from approximately 0 to 0.45. The pixel intensity values immediately outside the zone of dominant triaxiality were close to the boundary of the pixel intensities measured in the calibration lens. At the calibration lens boundaries, there is increased uncertainty in the calculated refraction angles. From Fig. 14(d), along centerline, $x = 0$ mm, the analytical solution for $\varepsilon_y = 0.002$ radians was approximately at $y = 9.01$ mm and the experimental result for the same refraction angle was at $y = 9.96$ mm; therefore, the difference in position was approximately 0.95 mm. There are also boundary effects impacting the outer isolines for the contours in

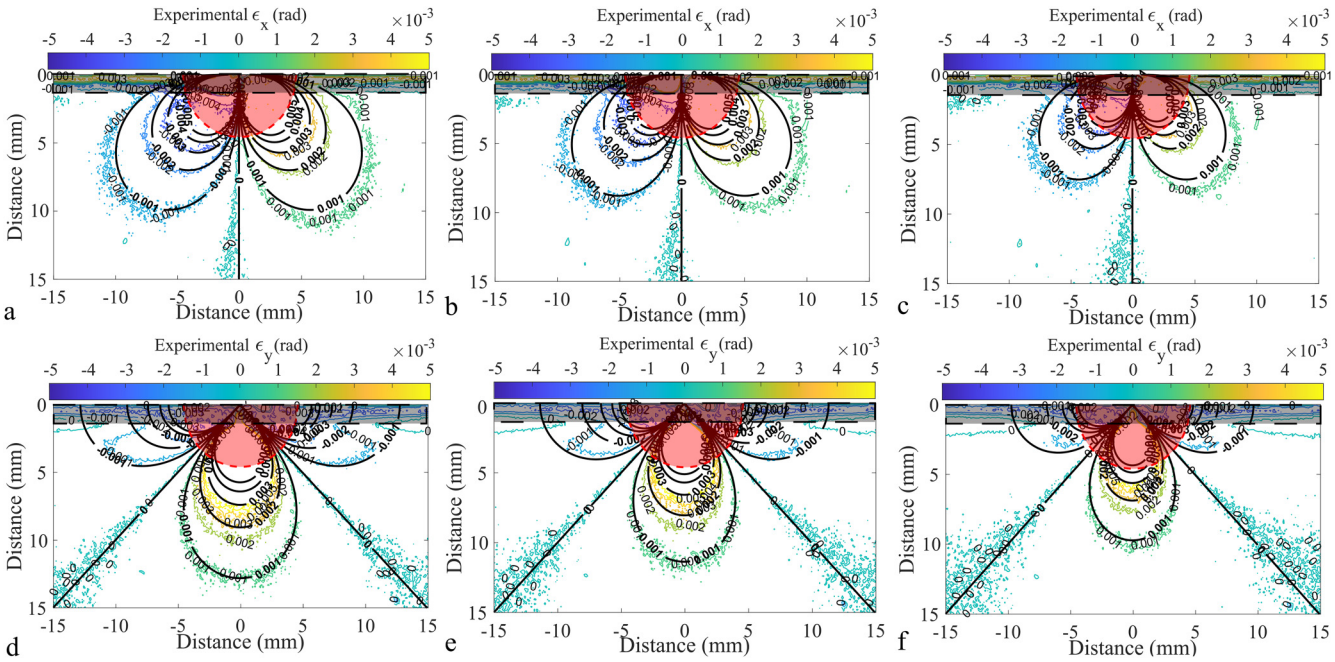

FIG. 14. The experimental refraction angles (colored contours) for (a)–(c) ε_x and (d)–(f) ε_y compared to the analytical solution (black) at compressive loads of (a) and (d) 2365 N $\pm$5 N, (b) and (e) 1860 N $\pm$5 N, and (c) and (f) 1360 N $\pm$5 N. The zone of dominant triaxiality is plotted as the red shaded area and boundary effects are highlighted in the gray shaded area. The contour levels are in radians.

Figs. 14(d)–14(f) which are caused by residual stresses in PMMA from the manufacturing process.

The refraction angles in the x- and y-directions were then used to estimate the radial stress, $\sigma_{rr} = (\sigma_{xx} + \sigma_{yy})$. Two different approaches were used to estimate the stresses. The first method used direct numerical integration of Eqs. (9) and (10) which requires knowledge of far field boundary conditions. If the far field boundary conditions are not known, then the second approach can be used leveraging the analytical solution. The expression of the Flamant solution was used here for the quasi-static tests because clear boundary conditions were not known. From the Flamant solution, the stress state, σ_{rr}, was estimated as[3]

$$\sigma_{rr} = (\sigma_{xx} + \sigma_{yy}) = \frac{\varepsilon_R}{C_\sigma d_e}(r\cos\theta), \tag{23}$$

where ε_R is the resultant refraction angle calculated from the experimentally measured refraction angles in the x- and y-directions using[3]

$$\varepsilon_R = \sqrt{\varepsilon_x^2 + \varepsilon_y^2}. \tag{24}$$

The Flamant solution can also be used to calculate ε_R from the applied force F at each radial position r,

$$\varepsilon_R = C_\sigma d_e \frac{2F}{\pi d_e r^2}. \tag{25}$$

Note that the specimen thickness d_e cancels in the theoretical relationship, but is shown for completeness from the derivation.

The resultant refraction angles and the corresponding stress contours for a compressive force of 2365 N $\pm$5 N are presented in Fig. 15. The resultant refraction angle compared to the analytical solution, Fig. 15(a), revealed some slight asymmetry from approximately -3 to 3 mm in the x-direction for refraction angles below 2 mrad. This is a result of the slight asymmetry in the horizontal cut-off data discussed previously. The outer isoline at $\varepsilon = 0.001$ radians aligns well with the analytical solution and the inner isolines are in agreement with the analytical solution above $x = 3$ mm and below $x = -3$ mm. As for the stress contours, Fig. 15(b), the experimental results do reveal noise in the data; however, the experiments are still in agreement with the analytical solution.

B. Experimental uncertainty

The primary experimental uncertainty was attributed to the calibration of the imaging system. There are two forms of calibration that were applied: a pixel-to-distance calibration and an intensity to refraction angle calibration. The uncertainty in the distance calibration was estimated at $\pm$0.05 mm which is based on a pixel uncertainty of $\pm$0.5 of a pixel. The second calibration process was the polynomial fit to the quantitative schlieren calibration lens pixel intensities. With respect to the pixel to meter calibration, the value for the location of a pixel intensity inside of the calibration lens was performed in pixels and converted to meters during the

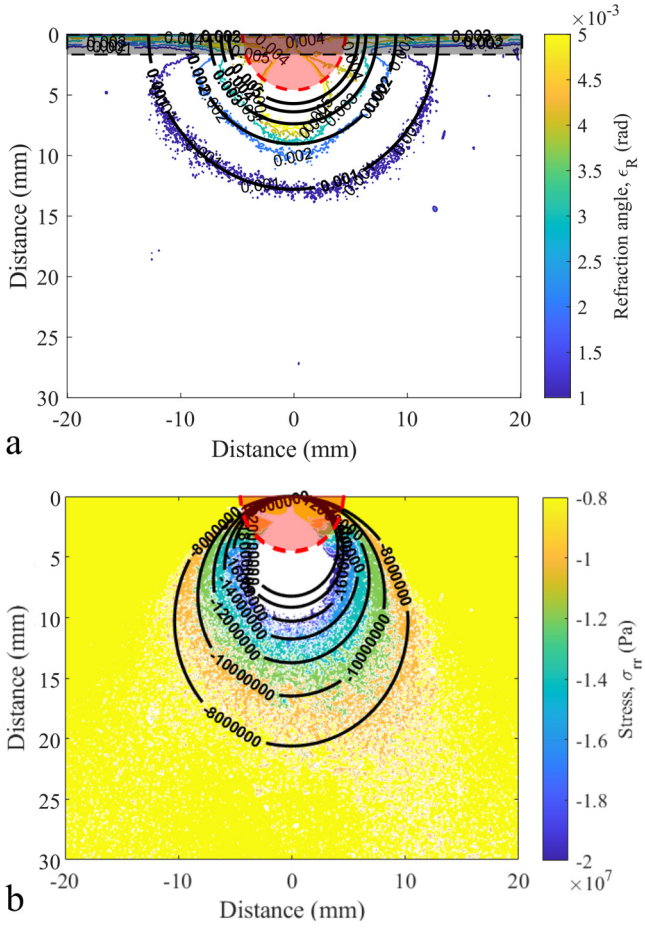

FIG. 15. (a) Resultant refraction angles and (b) stress contours for the experiments (colored contours) and the analytical solution (black contours) for a compressive force of 2365 N. The zone of dominant triaxiality is plotted as the red shaded area and the boundary effects in (a) are highlighted as the gray shaded area. The contour levels are in radians.

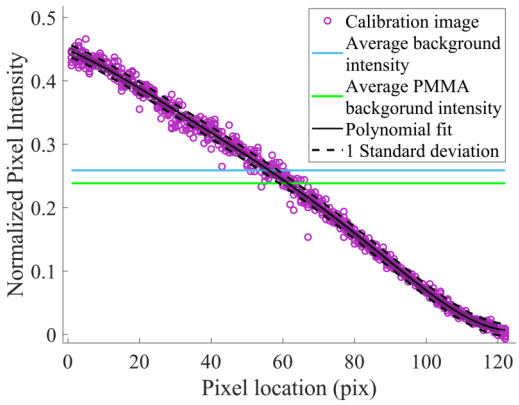

FIG. 16. Plot of the pixel intensity values (purple points) from the calibration lens with the polynomial fit (black line) along with the polynomial fit for $\pm\sigma_{SD}$ (dashed black line).

last step to reduce a compounding error. The resulting uncertainty in ε based on the uncertainty in the distance calibration was ± 0.02 mrad. The largest source of uncertainty was associated with the polynomial fit to the calibration lens.

The polynomial fit was used to determine a location in the calibration lens based on the pixel intensity in the experimental image. The average standard deviation for the polynomial fit to the calibration lens intensities was 0.0095, for pixel intensity values scaled from 0 to 1. To quantify the uncertainty based on one standard deviation variation, the polynomial fit was shifted by one standard deviation in both axes directions as shown by the dashed black lines in Fig. 16. The resulting refraction angles in the x- and y-directions, ε_x and ε_y, were then calculated with the shifted calibration curve. Figure 17 shows the resulting refraction angles by shifting the pixel intensities by (a) $+\sigma_{SD}$ and (b) $-\sigma_{SD}$.

The refraction angles calculated based on one standard deviation result in the experimental uncertainty bounding the analytical solution. Subtracting the refraction angles for $+\sigma_{SD}$ and $-\sigma_{SD}$ from the actual values of epsilon yields the uncertainty on a pixel-per-pixel basis. Subtraction of the two images results in a fairly consistent change in refraction angles resulting in an average refraction angle uncertainty of approximately -0.12 and 0.12 mrad, respectively.

C. Explosively driven shock wave experiments

The quantitative schlieren analysis based on the stress-optic law was extended to explosive induced shock experiments. For the shock studies, two synchronous high-speed cameras were used to visualize the event. The high-speed images were exposed by the pulsed laser illumination source at 15 ns, which eliminated the uncertainty in the temporal alignment of the two image sets. The two cameras had different knife-edge cut-off directions such that the refraction angles in the x- and y-directions were captured simultaneously. A vertical knife-edge cut-off was used to visualize the x-direction refraction angles, ε_x, and a horizontal knife-edge cut-off was used to visualize the y-direction refraction angles, ε_y. Images of the shock propagation through the PMMA are presented in Fig. 18 for (a)–(d) a vertical cut-off and (e)–(h) a horizontal cut-off.

A visual comparison of the two image sets shows that in the early time, $t < 12\,\mu$s, the shock in both image sets appears similarly. As time progresses, the differences in the schlieren images for the two knife-edge orientations become more apparent. In the last image before the shock impacts the free surface, $t \approx 37\,\mu$s, it is apparent that the refractions in the x-direction are stronger than the refractions in the y-direction, which was expected.

The dynamic range of pixel intensity values captured during the calibration process sets upper and lower limits for the refraction angles that can be calculated. Thus, it is important that the pixel intensities visualized in the calibration lens span the dynamic range of the camera sensor, which is 0–1 on a normalized pixel intensity scale. It was of particular importance for the calibration image

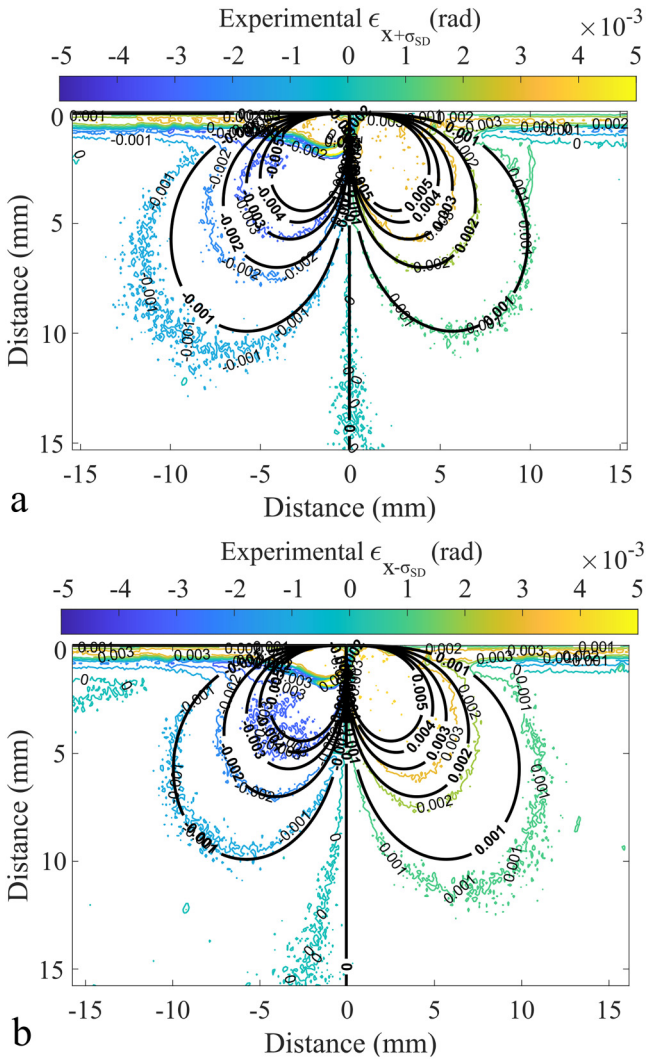

FIG. 17. Images of the refraction angles in the x-direction, ε_x, for (a) $+\sigma_{SD}$ and (b) $-\sigma_{SD}$, compared to the analytical solution for a compressive force of 2365 $\pm$5 N.

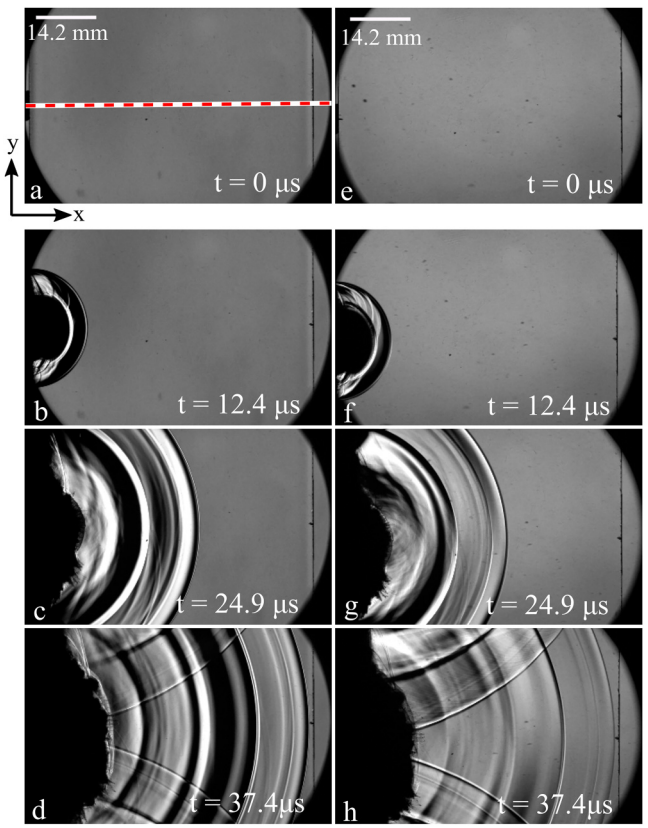

FIG. 18. Images of the shock propagation through a PMMA sample with (a)–(d) a vertical knife-edge cut-off and (e)–(h) a horizontal knife-edge cut-off. The time of each image relative to the detonator initiation is shown.

values to span the dynamic range of the camera sensor for the explosively induced shock experiments because shock waves are high pressure pulses which induce large light refraction angles. The calibration data for the vertical knife-edge cut-off images did capture the full dynamic range of the camera sensor. However, the maximum intensity value from the calibration data for the horizontal knife-edge cut-off images was approximately 0.96. Since the refraction angles that can be calculated are restricted by the intensity values inside of the calibration lens, any values outside of the pixel intensity values in the calibration lens were discarded in the analysis.

The resulting refraction angles from the shock experiments are calculated using the calibration lens pixel intensities as described above. Image intensities and the resulting refraction angles along centerline at the time and location of interest for the shock experiment are plotted in Fig. 19(c).

The intensity values plotted in Fig. 19(c), I_x and I_y, correspond to the lines plotted in the schlieren images of the shock propagating through the PMMA sample with a (a) vertical and (b) horizontal knife-edge cut-off, respectively. The plot of pixel intensities as a function of position compared to the refraction angles as a function of position shows that the pixel intensity and refraction angles follow the same trend, as expected. Thus, large changes in pixel intensity relative to the background correspond to large refraction angles. The background intensity of the undisturbed PMMA corresponds to the area of PMMA prior to the shock wave. In general, the displacements in the x-direction were much larger than the displacements in the y-direction, especially along the centerline, $y = 0$ mm, which was expected due to the wave propagation direction relative to the knife-edge direction.

For the vertical cut-off, I_x, there was a single high intensity pixel which was determined to be the shock wave front and is labeled as "shock front" in Fig. 19. The orientation of the knife-edge cut-off caused the shock wave to be detected as an

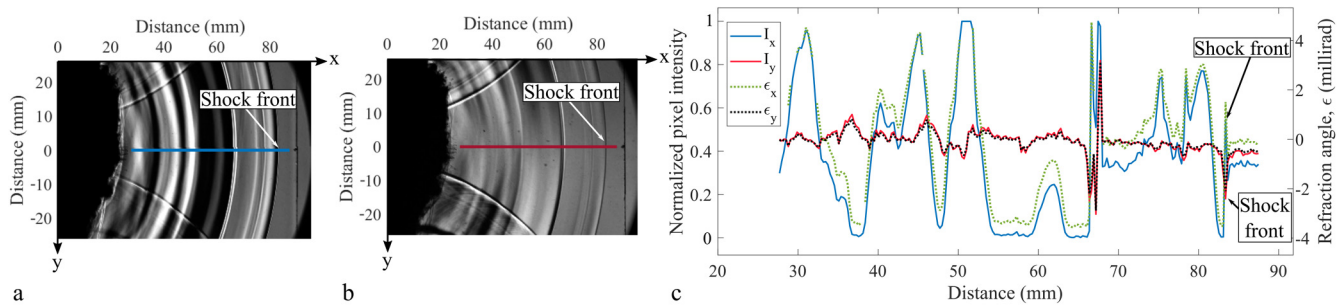

FIG. 19. Schlieren images of the explosively driven shock propagating through the PMMA sample at approximately 35 μs after detonation with (a) a vertical knife-edge cut-off and (b) a horizontal knife-edge cut-off with (c) a plot of the pixel intensities, I_x and I_y, and the calculated refraction angles, ε_x and ε_y, corresponding to the lines on (a) and (b).

intensity greater than the background pixel intensity, and the expansion behind the shock wave was detected as darker than the background. This was validated through comparison of the pixel intensities at different times from the digital streak image presented in Fig. 20. The digital streak image presented in Fig. 20(a) was created by extracting the centerline row of pixels indicated as the dashed red line in Fig. 18(a) from every image in the data set and stacking them vertically such that time was on the y axis and distance was on the x axis. The segments of the pixel intensity values at three different times from the digital streak image were extracted and plotted in Fig. 20(b). The position of pixel intensity values extracted were aligned such that the position of the shock front was at $x_s = 0$ mm.

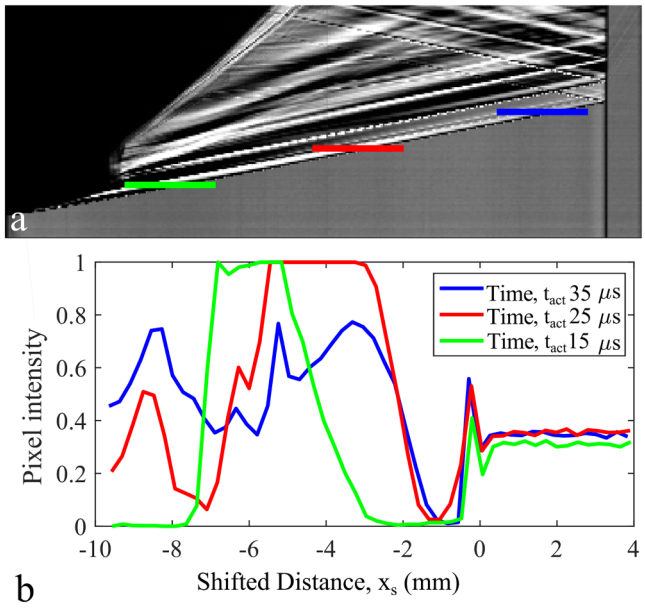

FIG. 20. (a) A digital streak image for the vertical cut-of data with segments indicating the rows of pixels extracted. (b) The pixel intensity values detected for the shock wave along the green ($t_{act} = 15\mu$s), red ($t_{act} = 25\mu$s), and blue ($t_{act} = 35\mu$s) lines.

The row of pixels along the centerline of the PMMA sample was extracted from the digital streak image at a time of $t = 35.5\mu$s for the calculation of the stress through the shock field. This time was chosen because it was before the shock impacted the PMMA boundary at $t = 38\mu$s, which allows the numerical integration to be applied from the far field with known boundary conditions, i.e., undisturbed PMMA. This time was also chosen because it was before the shock entered a region near the PMMA boundary where a slight stress gradient due to residual stresses from the manufacturing process was observed. This residual stress region spanned approximately eight pixels inward from the boundary and is visualized in the digital streak images presented in Fig. 20(a).

Numerical integration of the refraction angles, ε_x, was performed from the undisturbed PMMA through the shock wave to determine the stress state at a given location. Rearranging Eq. (9) to solve for stress $(\sigma_{xx} + \sigma_{yy})$ yields

$$\sigma_{xx} + \sigma_{yy} = \frac{1}{C_\sigma d_e}\int \varepsilon_x dx. \tag{26}$$

Plane stress is assumed which allows for σ_{yy} to be expressed in terms of σ_{xx} using Poisson's ratio, ν, as

$$\sigma_{yy} = \frac{\nu}{1-\nu}\sigma_{xx}. \tag{27}$$

Equation (26) then becomes

$$\sigma_{xx} = \frac{1-\nu}{C_\sigma d_e}\int \varepsilon_x dx. \tag{28}$$

The numerical integration of the refraction angle was performed using the trapezoid method over the distance between pixels and is presented in Fig. 21. Integration of the refraction angle caused the detected shock wave to be completely lost during the integration process because it was only observed in one pixel. However, the negative phase of the shock wave was still present after integration. Integrating the refraction angle, ε_x, to estimate the stress gradients from the schlieren images leverages the stress-optic

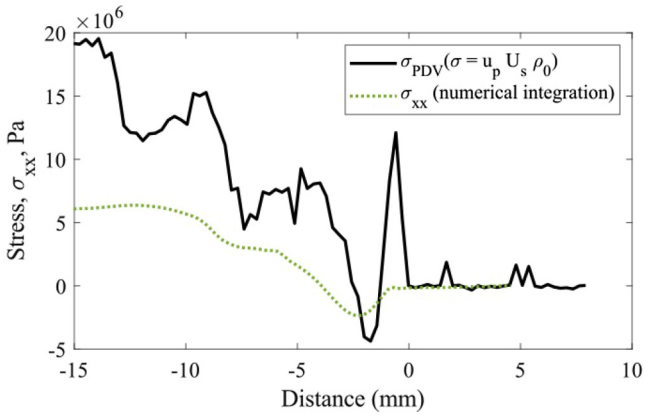

FIG. 21. A plot of the mean stress calculated from the surface velocity measurements and the stress calculated by numerical integration of refraction angle. Note that the sign convention for the compressive stress is opposite than the normal convention.

law, but the explosive induced shock is a large stress gradient which violates the assumption of small stress gradients and small refraction angles when relating the light propagation vector to the change in optical path length [Eq. (8)]. The integration, however, was still performed and compared to the stress calculated using PDV shown in Fig. 21. The resulting stresses, although not the same, follow a similar trend.

The PDV measurement, made at the free surface in line with the centerline pixel row, was used to calculate the induced stress field as plotted in Fig. 21. PDV measurements yield a surface velocity history, i.e., surface velocity as a function of time. For comparison to the schlieren images, time was converted to distance using the average shock velocity.[18] The shock velocity was calculated using the digital streak image in Fig. 20. The boundary of the shock wave visualized in the digital streak image was extracted using MATLAB. A linear fit was applied to the extracted shock front to which the slope of the linear fit, 2.83 mm/μs, was used as the average shock velocity. The surface velocity as a function of distance was reflected over the x axis at an x-distance of approximately 88 mm which was the distance the shock wave traveled in the PMMA. The stress calculated using the PDV signal, σ_{PDV}, was approximated using the measured surface velocity, u_{sf}, shock velocity, U_s, and bulk density, ρ_0,

$$\sigma_{PDV} = \frac{u_{sf}}{2} U_s \rho_0. \tag{29}$$

The two data sets in Fig. 21 were aligned by shifting the distance axis based on the location of the shock front such that $x_s = 0$ mm was the location of the shock front.

The schlieren and PDV data show the same trends; however, the shock wave is better resolved in the PDV measurement than the high-speed imaging. The shock rise time in the PDV measurements, calculated from $u_{sf} = 0$ m/s to $u_{sf} = 7.2$ m/s, occurred over approximately 0.20 μs. The image resolution on the high-speed cameras was approximately 0.3 mm/pixel. With the shock wave traveling at approximately 2.83 mm/μs and an illumination pulse of 15 ns, the shock is smeared over approximately 0.15 pixels. The rise time from the PDV of 0.2 μs spans approximately 1.8 pixels. The high-speed camera, thus, does not have sufficient pixel resolution at this magnification to accurately resolve the shock wave pulse to the fidelity that the PDV does. The refraction angle data for the shock are, thus, expected to be limited in the shock here because of how thin and fast it is.

D. Discussion

Quantitative schlieren analysis has been demonstrated to be viable for measuring stress fields in transparent solids. This technique can be applied similarly to the traditional techniques of photoelasticity, coherent gradient sensing, and digital gradient sensing. The quantitative schlieren technique is most similar to DGS, and the governing equations used for the analysis are the same.[2,3] Both methods yield the same result with no requirement to analyze fringes, as in photoelasticity and CGS.

To experimentally determine the stress gradients in both the vertical and horizontal directions, the quantitative schlieren analysis requires images of both horizontal and vertical cut-offs, respectively. This is similar to CGS which requires two sets of diffraction gratings to capture stress gradients in both directions. Capturing both gradients using either technique can be performed with two cameras simultaneously, as done here, or sequentially using a single camera and changing the cut-off orientation between images. DGS analysis yields the two-dimensional light ray refraction directly from a single test image compared to a baseline pre-test image of a speckle background, thus providing the ability to measure stress gradients in any in-plane direction without the need to adjust the experimental configuration. The quantitative schlieren analysis yields a stress gradient measurement on a pixel-to-pixel basis whereas DGS leverages Digital Image Correlation (DIC) such that the stress gradient measurements are calculated using, and averaged over, a correlation window.

Quantification of the uncertainty for DGS is limited, as the uncertainty is based on the digital image correlation uncertainty which is difficult to quantify directly.[23] The uncertainties presented here for the quantitative schlieren analysis were directly propagated through the calculation process which does not involve a correlation process. In both methods, the uncertainty is primarily a function of the camera resolution, with a higher resolution camera yielding a more precise result. The calibration lens choice is critical for the quantitative schlieren analysis where the lens refraction angles define the quantitative range of the system. In DGS, the physical setup geometry, including the distance from the sample to the background pattern and the background pattern speckle size and density, governs the refraction angles that can be quantified. Calibration of the system requires precise measurement of the setup geometry or measurement of a known refraction, similar to the use of the calibration lens in quantitative schlieren. Both methods can resolve similar refraction angles in general.

Since DGS is a direct imaging method, non-parallel light results in perspective within the images. The schlieren analysis utilizes parallel light so geometry is represented on a one-to-one basis. Quantitative schlieren is most restricted by the size of the optics

required, with schlieren lenses or mirrors readily available up to only ≈30 cm. DGS can be applied on a near infinite scale, limited only by the size of a background and camera lenses available.

VII. CONCLUSION

Quantitative schlieren imaging has been extended here to measure refraction angles and stress states in optically transparent PMMA. Quasi-static and dynamic experiments were preformed. Refraction angles measured from the schlieren images were used to estimate the stress state of the PMMA using the stress-optic law. The derived equations using the stress-optic law relate the refraction angles to the stress gradients.

The experimental arrangement for the quasi-static experiments allowed for the analytical Flamant solution to be used to estimate the stress state of the material. The comparison between the experimental refraction angles and the analytical refraction angles for the quasi-static experiments validated the quantitative schlieren analysis. The schlieren lens calibration data were found to have a significant impact on the measurable data and to be the largest source of uncertainty for this method.

Due to limited image resolution with the high-speed cameras in the dynamic experiments, the shock wave was not adequately resolved to allow spatial measurement of the stress field through the shock itself. Only a singular pixel of the shock was visualized in the images; therefore, when integrating the refraction angles to estimate stress, the shock wave was fully lost. However, the wave structures behind the shock wave were captured and followed the same trend as the stresses calculated from the PDV measurements.

The analysis and experiments presented here show that the quantitative schlieren analysis can be used to estimate stresses in transparent materials, and the calibration process and image resolution are the most important sources of potential error and limitations of applicability.

ACKNOWLEDGMENTS

Portions of this work were supported by DOE-NNSA MSIPP (Award No. DE-NA0003988) and AFOSR (Grant No. FA9550-19-1-0379).

AUTHOR DECLARATIONS

Conflict of Interest

The authors have no conflicts to disclose.

Author Contributions

S. M. Torres: Data curation (equal); Formal analysis (equal); Investigation (equal); Methodology (equal); Writing – original draft (lead); Writing – review & editing (equal). **J. Kimberley:** Conceptualization (equal); Funding acquisition (equal); Investigation (equal); Methodology (equal); Project administration (equal); Supervision (equal); Writing – review & editing (equal). **M. J. Hargather:** Conceptualization (equal); Funding acquisition (equal); Investigation (equal); Methodology (equal); Project administration (lead); Supervision (equal); Writing – review & editing (equal).

DATA AVAILABILITY

The data that support the findings of this study are available from the corresponding author upon reasonable request.

REFERENCES

[1]A. S. Kobayashi, *Handbook on Experimental Mechanics*, 2nd ed., edited by A. S. Kobayashi (VCH, New York, 1993).
[2]C. Periasamy and H. V. Tippur, "Measurement of orthogonal stress gradients due to impact load on a transparent sheet using digital gradient sensing method," Exp. Mech. **53**, 97–111 (2012).
[3]C. Periasamy and H. V. Tippur, "Full-field digital gradient sensing method for evaluating stress gradients in transparent solids," Appl. Opt. **51**, 2088 (2012).
[4]E. E. Gdoutos, "The method of caustics," in *Solid Mechanics and Its Applications* (Springer International Publishing, 2021).
[5]Z. Yue, P. Qiu, R. Yang, S. Zhang, K. Yuan, and Z. Li, "Stress analysis of the interaction of a running crack and blasting waves by caustics method," Eng. Fract. Mech. **184**, 339–351 (2017).
[6]W. Xu, X. Yao, H. Yeh, and G. Jin, "Fracture investigation of PMMA specimen using coherent gradient sensing (CGS) technology," Polymer Test. **24**, 900–908 (2005).
[7]H. V. Tippur, "Coherent gradient sensing (CGS) method for fracture mechanics: a review," Fatigue Fract. Eng. Mater. Struct. **33**, 832–858 (2010).
[8]E. E. Gdoutos, "The optical method of caustics," Opt. Lasers Eng. **79**, 68–77 (2016).
[9]H. V. Tippur, S. Krishnaswamy, and A. J. Rosakis, "A coherent gradient sensor for crack tip deformation measurements: Analysis and experimental results," Int. J. Fract. **48**, 193–204 (1991).
[10]H. V. Tippur, S. Krishnaswamy, and A. J. Rosakis, "Optical mapping of crack tip deformations using the methods of transmission and reflection coherent gradient sensing: A study of crack tip k-dominance," Int. J. Fract. **52**, 91–117 (1991).
[11]A. Rosakis, "Application of coherent gradient sensing (CGS) to the investigation of dynamic fracture problems," Opt. Lasers Eng. **19**, 3–41 (1993).
[12]G. S. Settles and M. J. Hargather, "A review of recent developments in schlieren and shadowgraph techniques," Meas. Sci. Technol. **28**, 042001 (2017).
[13]M. Raffel, "Background-oriented schlieren (BOS) techniques," Exp. Fluids **56**, 60 (2015).
[14]G. S. Settles and A. Liberzon, "Schlieren and BOS velocimetry of a round turbulent helium jet in air," Opt. Lasers Eng. **156**, 107104 (2022).
[15]B. Atcheson, W. Heidrich, and I. Ihrke, "An evaluation of optical flow algorithms for background oriented schlieren imaging," Exp. Fluids **46**, 467–476 (2008).
[16]G. S. Settles, *Schlieren and Shadowgraph Techniques* (Springer Berlin Heidelberg, 2001).
[17]M. J. Hargather and G. S. Settles, "A comparison of three quantitative schlieren techniques," Opt. Lasers Eng. **50**, 8–17 (2012).
[18]J. D. Tobin and M. J. Hargather, "Quantitative schlieren measurement of explosively-driven shock wave density, temperature, and pressure profiles," Propellants Explos. Pyrotech. **41**, 1050–1059 (2016).
[19]P. Podio-Guidugli and A. Favata, "The flamant problem," in *Solid Mechanics and Its Applications* (Springer International Publishing, 2013).
[20]S. Timoshenko and J. Goodier, *Theory of Elasticity*, 3rd ed. (McGraw-Hill Book Company, 1970).
[21]O. T. Strand, D. R. Goosman, C. Martinez, T. L. Whitworth, and W. W. Kuhlow, "Compact system for high-speed velocimetry using heterodyne techniques," Rev. Sci. Instrum. **77**, 083108 (2006).
[22]I. Daniel Dolan and T. Ao, "SIRHEN: A data reduction program for photonic doppler velocimetry measurements," Technical Report SAND2010-3628 (Sandia National Laboratories, 2010).
[23]International Digital Image Correlation Society, E. M. C. Jones, and M. A. Iadicola, *A Good Practices Guide for Digital Image Correlation* (International Digital Image Correlation Society, 2018).